Modeling of wind-induced fatigue of cold-formed steel sheet panels

Osvaldo Rosario-Galanes[1a] and Luis A. Godoy[*2]

[1]*Department of Civil Engineering, University of Puerto Rico, Mayaguez, Puerto Rico*
[2]*Structures Department, FCEFyN, National University of Córdoba, and CONICET,
P.O. Box 916, Córdoba 5000, Argentina*

Abstract.   Wind-induced failure around screwed connections has been documented in roof and wall cladding systems made with steel sheet cold-formed panels during high wind events. Previous research has found that low cycle fatigue caused by stress concentration and fluctuating wind loads is responsible for most such failures. A dynamic load protocol was employed in this work to represent fatigue under wind effects. A finite element model and fatigue criteria were implemented and compared with laboratory experiments in order to predict the fatigue failure associated with fluctuating wind loads. Results are used to develop an analytical model which can be employed for the fatigue analysis of steel cold-formed cladding systems. Existing three dimensional fatigue criteria are implemented and correlated with fatigue damage observed on steel claddings. Parametric studies are used to formulate suitable yet simple fatigue criteria. Fatigue failure is predicted in different configurations of loads, types of connections, and thicknesses of steel folded plate cladding. The analytical model, which correlated with experimental results reported in a companion paper, was validated for the fatigue life prediction and failure mechanism of different connection types and thicknesses of cold-formed steel cladding.

Keywords: cold-formed plates; connections; dynamic load protocol; fatigue failure; finite element analysis; folded plates; steel; wind

1. Introduction

Wind-induced damage and failure of roof and wall steel cladding in industrial buildings and storehouses has been frequently reported in the tropics and other regions prone to high winds or hurricanes/cyclones. Because such failures are of great concern to designers, insurance companies, and mitigation agencies, research in this field has been approached from various perspectives. On the one hand, fatigue damage and failure estimates of steel cladding systems based on empirical methods and field observations led to the development of fragility curves (see, for example, Lee and Rosowsky 2004, López and Godoy 2005). On the other hand, considerable effort has also been made on experimental and analytical estimates of static and fatigue failure under wind simulations.

Early observations and analytical models focused on static failure of steel cladding systems.

---

*Corresponding author, Professor, E-mail: lgodoy@efn.uncor.edu
[a]M.S., E-mail: ingenierorosario@gmail.com

Studies by Beck and Stevens (1979), Mahendran (1995) showed that stress concentrations around the connections are responsible for low cycle fatigue failure. Mahendran and Mahaarachchi (2002) conducted small-scale constant amplitude load tests of steel cladding connections and compared their results with static failure loads. They developed simple equations relating the static failure load to constant amplitude loads, and also performed multilevel cyclic test and proposed a modification factor to be used on Miner's rule in order to predict fatigue damage for variable amplitude loading.

More recent investigations (Mahaarachchi and Mahendran 2008) extensively evaluated the splitting resistance of steel claddings of different geometrical shapes and material properties, postulated a strain criterion, and evaluated design equations based on their findings. The results show that the cross-sectional geometry of folded plates plays a critical role on the static behavior. Such investigations have been successful in determining a strain criterion and design formula for static pull-through failures in some crest-fixed steel claddings (Mahaarachchi and Mahendran 2008, 2009). Recent models addressing steel cladding systems focused on Australian construction practices, in which claddings are made of thin, high strength G550 steel and are crest-fixed.

Although there is a wealth of information about wind induced failure of steel cladding systems, research is still needed to account for building practices in the US coastal areas and the Caribbean region. New studies are needed to consider valley-fixed steel claddings and cyclic loading in developing a working analytical model.

Equations have been developed to relate static failure loads and fatigue damage loads; however, these equations are only applicable to a limited number of steel cladding configurations and materials. In order to be able to predict fatigue damage in more general situations, it is necessary to establish a methodology that accounts for the fatigue properties of different materials and is based on analytical models of the stresses and strains that are responsible for fatigue failure.

In a companion paper, García-Palencia and Godoy (2013) reported experimental studies to assess the fatigue strength of wall and roof claddings. Testing was conducted on commercially available cold-formed steel panels commonly employed in the construction of industrial buildings. The panels were fixed to a supporting frame by means of self-drilling screws. In some configurations, the panels were fixed at the valleys, whereas crest-fixed connections were also investigated. The use of washers to reinforce the connections was also investigated. A hydraulic load actuator was used to apply the load with a digital function generator to simulate the effect of pressure induced by wind as a sinusoidal function. The load was transferred to the panel by means of 12 cubic air bags, which were located between the load plate and the panel. The load protocol originally developed by Baskaran *et al*. (2006) was followed in order to investigate wind-induced fatigue.

This paper reports results of an analytical investigation based on finite element modeling and three dimensional fatigue criteria on some of the configurations considered in the experiments of García-Palencia and Godoy (2013). The paper is organized as follows: Section 2 presents the structural configuration considered and the dynamic load protocol followed in the computations. The structural analysis of the panel under static pressures is reported in Section 3. The resulting stress and strain fields are used in Section 4 as the bases of fatigue analysis. Results are presented in Section 5 to illustrate the methodology and compare alternative fatigue criteria. Conclusions are drawn in Section 6.

2. Structural configuration and load protocol

2.1 Structural configuration considered

The analytical investigation reported in this paper attempts to model the class of failure of connections observed in experiments on cold-formed steel panels.

The configuration considered is a two-span steel folded plate shown in Fig. 1, with overall dimensions 3.35m in length and 0.96m in width. The dimensions correspond to full-scale cladding commercially available from a manufacturer (Matcor 2007), which were used for the experiments. The cross section is a wide rib Type B deck, also shown in Fig. 1, with six valleys (each of 89mm width) and five crests of 44mm.

The decks are cold-formed from galvanized steel conforming to ASTM specification A653 (ASTM 2009). Three thicknesses were considered, i.e. 0.759mm, 0.912mm, and 1.214mm, which correspond to deck gauges 22, 20, and 18 respectively.

Three cases of connections are considered for the same geometry: screwed connections in valleys (illustrated in Fig. 2(a)), screwed connections in crests (Fig. 2(b)), and washer-reinforced connections in valleys, for a total of 12 combinations of thicknesses and connections, as shown in Table 1. Notice that 24 configurations were investigated in the experiments of García-Palencia and Godoy (2013), as shown in Column 2 of Table 1; however not all of them failed within the test physical limits.

2.2 Dynamic load protocol

The SIDGERS dynamic load protocol (Baskaran *et al*. 2006), which was used by García-Palencia and Godoy (2013) to conduct laboratory testing, has been implemented for this analytical investigation.

The SIDGERS Group in Canada (Baskaran *et al*. 2006, 2012) proposed the use of a dynamic load protocol to evaluate fatigue behavior under a wind load simulation. A number of levels (identified as level A, B, C, D, E, … in Fig. 3) are defined in this protocol, each consisting on two groups of oscillations (identified as Group 1 and Group 2 in Fig. 3) with various stress amplitudes and mean stress. Cycles in Group 1 simulate suction due to wind on the roof of an industrial building; whereas cycles in Group 2 represent the effect of exterior wind fluctuations combined with constant interior pressure in the building.

In SIDGERS, one can choose a reference load (indicated in Column 5, Table 1), and the test goes through several levels until failure is reached. This allows classification of the fatigue strength of a component as the last complete group that has been passed without failure. For example, if a sample completes level B for a reference load P, then it is given a classification equal to 1.25P.

The protocol adopted for the computations reported in this work is the same employed in the tests (Garcia-Palencia and Godoy 2013).

The general strategy of analysis requires performing a stress analysis at each load sublevel considered, and a fatigue analysis to identify if failure has already occurred. However, while García-Palencia and Godoy (2013) recorded first connection failure and continued the tests until three connections failed in an attempt to represent collapse of the specimen, the analytical results reported in this paper are limited to failure of the first connection. Modeling progressive failure of at least three connections, as was done in the tests, would require a more involved computational analysis that would be far from the possibilities available to a designer.
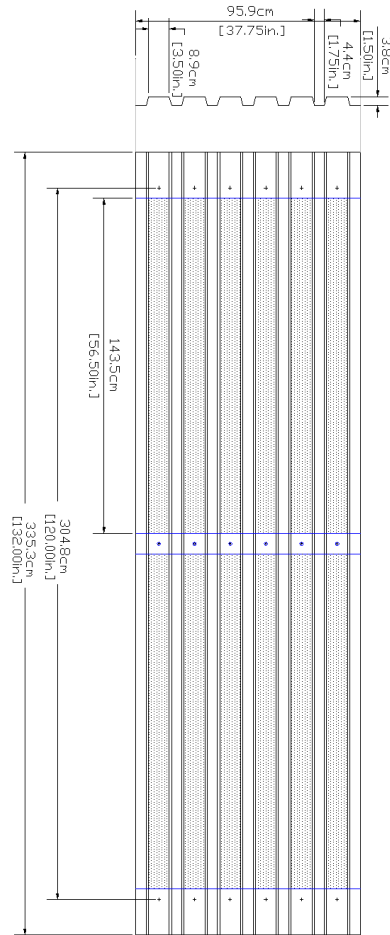
Fig. 1 Two-span steel panel considered. Cross section is Type B (Matcor 2007)

Table 1 Configurations considered by García-Palencia and Godoy (2013)

Model	Configuration # in tests	Deck Gauge	Screw Locations (Fig. 1(b)-(c))	Load P (kip)	Load P (MN)
1	3	22	1-2-3-4-5-6 (valleys)	2.0	0.00889
2	4	22	1-3-4-6 (valleys)	1.0	0.00444
3	5	22	1-2-3-4-5-6 (valleys-washer)	2.0	0.00889
4	6	22	1-3-4-6 (valleys-washer)	2.0	0.00889
5	13	18	1-3-4-6 (valleys)	1.5	0.00666
6	15	20	1-3-4-6 (valleys)	1.5	0.00666
7	17	20	1-3-4-6 (valleys-washer)	1.5	0.00666
8	18	18	1-3-4-6 (valleys-washer)	2.5	0.0111
9	19	18	1-2-3-4-5 (crests)	1.0	0.00444
10	20	20	1-3-5 (crests)	1.2	0.00532
11	21	22	1-3-5 (crests)	1.2	0.00532
12	24	18	1-3-5 (crests)	1.2	0.00532
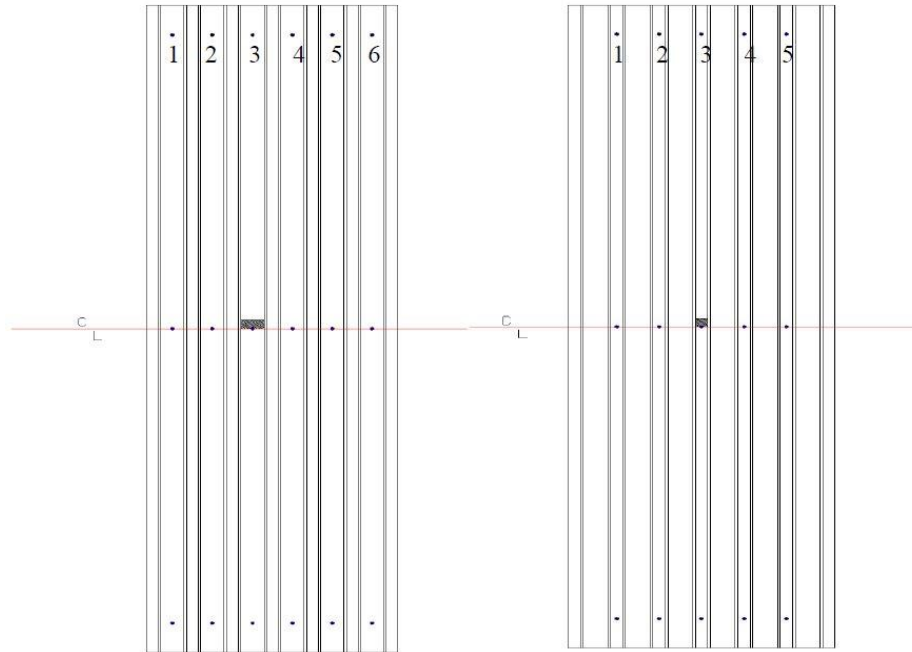
Fig. 2 Connections at the steel panels considered (a) Identification of screwed connections (1-6) at valleys and (b) Identification of screwed connections (1-5) at crests
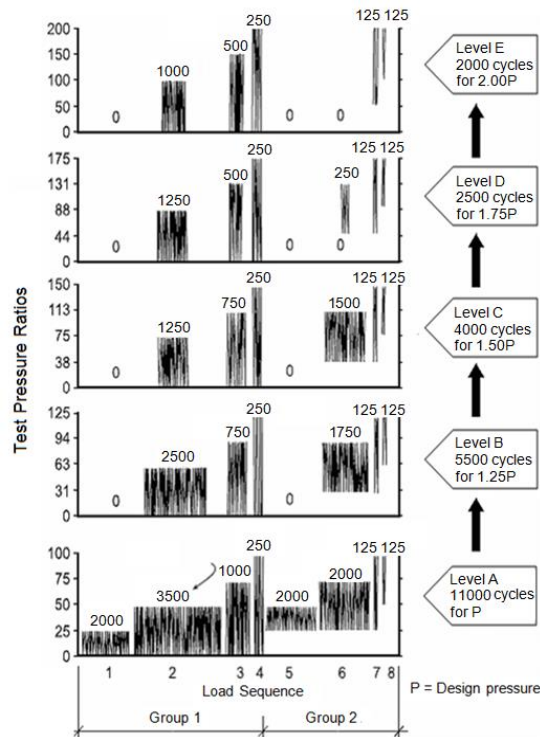
Fig. 3 Load sequence used in SIDGERS protocol (Adapted from Baskaran *et al*. 2006)

3. Evaluation of stress field in a panel

Results for a single geometry of folded plate configuration are reported in detail, together with the influence of several parameters, such as the thickness of the cladding and the spacing and type of connections. Modeling of this problem is divided into two parts: first, a static stress analysis of the complete panel is carried out by means of finite element analysis; second, a local fatigue analysis is performed at critical points around connections (Section 4).

3.1 Finite element model

In the first part of this research, a finite element model of the panel has been carried out to evaluate the static stresses and strains caused by wind pressures. The general purpose finite element code ABAQUS (2008) was used in the computations. Quadratic quadrilateral S8R and triangular STRI65 shell elements from the ABAQUS element library were used to perform the analyses.

3.2 Domain considered in the analysis

Because of symmetry considerations, only one fourth of the cladding described in Fig. 1 is modeled, as shown in Fig. 4.

Screw holes are defined in detail only at the center of the panel, where the plate screws take most of the load, and the location where the panel fails during the tests. Center holes at the right of Figure 4 are defined by creating a circular extrusion cut with radius defined as the inner radius in Fig. 5(a). At the center holes, displacement restrictions on three orthogonal directions are defined on the circumference of the circle around the hole (outer radius defined in Fig. 5(a)). This circumference defines the contour of the screw head, which is responsible for the lateral reaction force per unit length in the plate. In washer reinforced connections, this circumference defines the washer, which has a radius of 19.1mm, under the assumption that the washer is stiffer than the plate. Detailed modeling of the screw and washer has not been carried out in this work because failure in the reported experiments occurs on the steel cladding and not on the screw itself.

Refinement of the geometry of the plate near the holes with lower values of load than the center holes was not considered to be necessary because stress and strain variations near a hole do not affect the stress fields around the other holes. On the remaining screws, the reaction force is assumed to be a point load.

3.3 Loading system

The load was modeled as a pressure acting normal to a plane perpendicular to an axis passing through the center of the screws. The shaded regions in Figs. 1 and 4 represent the area where wind pressure is applied, and the cutting lines in Fig. 4 represent axes of symmetry. Pressures were not applied on the entire surface because the objective was to model the experimental setup performed by García-Palencia and Godoy (2013), in which airbags were positioned on the surface below the cladding. Airbags were mostly rigid having contact only at the outermost surface.

Starting from the first loading sublevel of the loading protocol, the load magnitude is defined for each sublevel for which the load exceeds the previously applied maximum load. Thus, a number of static finite element analyses are made as the load progresses in the protocol of Fig. 3.
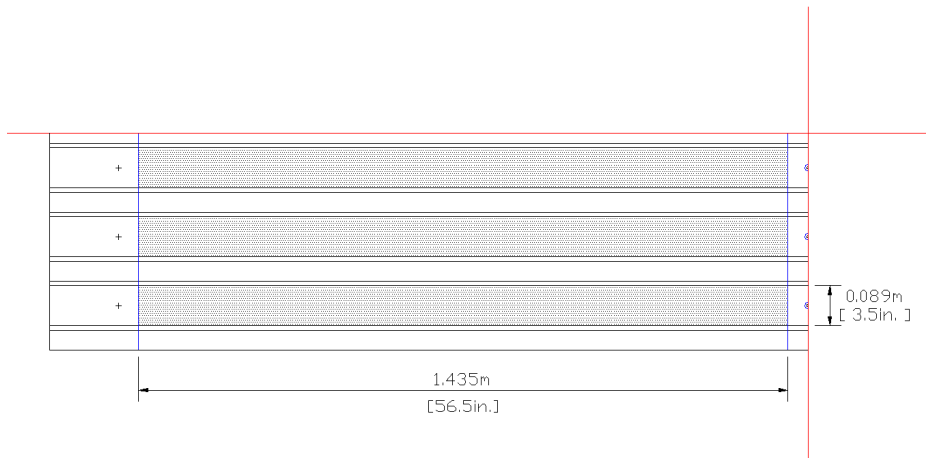
Fig. 4 Geometry of the panel area discretized using finite elements
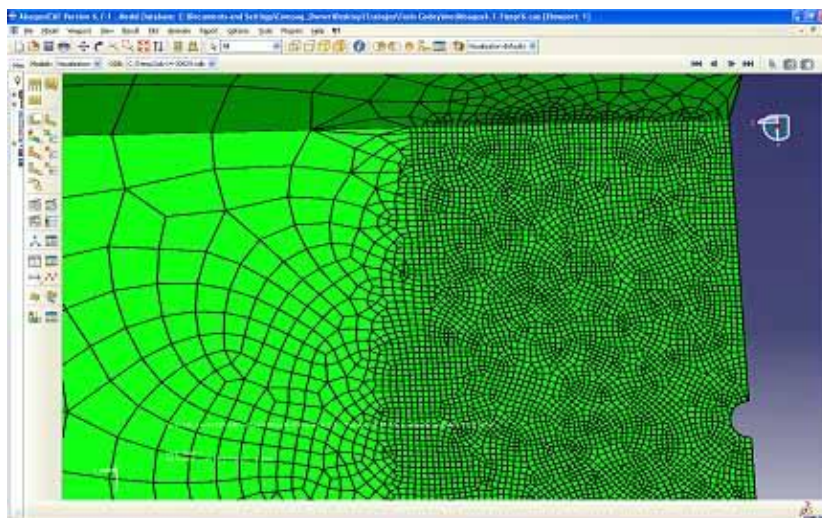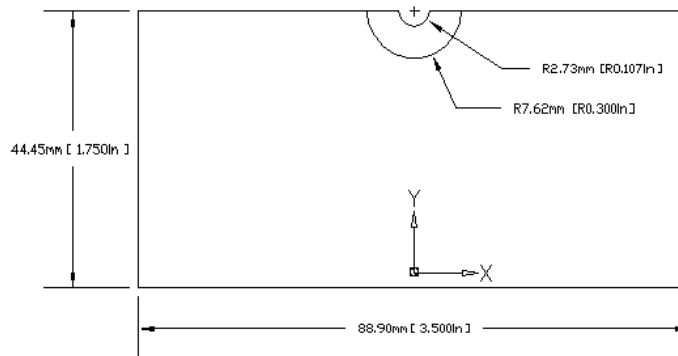
Fig. 5 Detail of a center connection from the shaded region in Fig. 2 (a) Geometry of the region, (b) Finite element mesh in the region of the connection

3.4 Constitutive material models

Static results were computed for two different material models. In the first model, the material was defined as linearly elastic-perfectly plastic, with modulus of elasticity E = 200GPa, Poisson's ratio v = 0.3, and yield stress σ_y = 228MPa. The von Mises yield function was used to account for multi-axial stress states.

In the second model, a linear strain-hardening zone is added with hardening modulus of 2GPa after a strain of 0.02 and extending to a failure strain of 0.20 and true fracture stress of 590MPa. The ultimate tensile strength of the material is 311MPa per ASTM A-653. The true fracture stress, which accounts for reduction in area, was approximated from the universal slopes method (Manson 1965) as 1.9 times the ultimate tensile strength (311MPa) which yields 590MPa.

The strain at which the strain-hardening region begins is taken to be 15 to 20 times the maximum elastic strain (Salmon *et al*. 2009). Although realistic material behavior has a limit of linear behavior lower than the yield strength, the flow stress starts at 2% strain, which is in good agreement with the elastic-perfectly plastic assumption (ASTM 2009).

In the linear analysis the material is defined as elastic and with linear kinematic (strain-displacement) relations. Kinematic nonlinearity is used to account for large displacements/rotations in the nonlinear analysis.

3.5 Finite element mesh

Elements with a random distribution are defined in order to make a transition from the circular geometry of the hole to the rectangular geometry of the span. An irregular finite element mesh has been used where changes in geometry do not allow a regular mesh pattern. A more refined distribution is assigned to a square region of 88.9mm defined in Fig. 5 surrounding the center screwed connections. The general pattern of the mesh being more refined closer to the center holes is made to take into account the stress concentration near the holes, as shown in Fig. 5 and suggested by previous studies (Mahaarachchi and Mahendran 2004). Refinement of the mesh is carried out by increasing the total number of elements on the partition and then on the squared regions along the center holes. Five mesh refinements were considered and convergence was achieved between 12,000 and 20,000 elements by increasing the total number of elements from 1,082; 7,715; 12,827; 20,742; and 30,929. As a result of the convergence study, a mesh of about 20,000 elements with size of 1mm near the connections was used in the computations reported in this paper, which is consistent with similar mesh sensitivity studies performed by other authors (Prinz and Nussbaumer 2012).

The outcome of this analysis is the evaluation of the highest stresses and strains at the most critical connection in a panel at a given load sublevel. The results are listed in Table 2 for Configuration #3. The total area under pressure in Fig. 1 is 1.532 m^2, of which ¼ (or 0.383 m^2) is considered in the finite element discretization of Fig. 4. Thus, the pressure acting in Fig. 4 at loading sublevel A4 with a load P of 0.00889 MN is 0.00581 MPa, which is listed in the second column of Table 2.

4. Fatigue analysis of a connection

The previous static analyses were performed to evaluate stress and strain fields around a critical

Table 2 Static analysis results of Configuration #3 in Table 1 for elastic-plastic material

Sublevel	Pressure (MPa)	S, von Mises (MPa)	S, Max (MPa)	ε, Max $\times 10^{-3}$
A1	0.001453	227.5	259.4	4.049
A2	0.002905	227.5	258.8	10.55
A3	0.004358	227.5	258.8	16.60
A4	0.005810	227.5	258.8	
B4	0.007263	227.5	258.8	
C4	0.008715	227.5	258.8	
D4	0.010168	227.5	258.8	
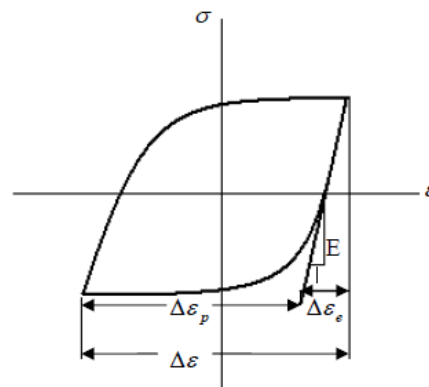
Fig. 6 Completely reversed loading cycle ($R = -1$)

connection, and they are next employed to carry out fatigue analysis using analytical (rather than finite element) models.

4.1 Loading cycle

For a completely reversed fatigue process, a loading cycle may be composed of elastic and plastic deformation, as shown in Fig. 6, where $\Delta\varepsilon_p$ is the plastic strain component and $\Delta\varepsilon_e$ is the elastic component. For the present case it is assumed that loading is not completely reversed and instead the stress ratio $R = 0$ is used for tension loading at the bottom of the plate (pressure side). As a result, only the first quadrant in Fig. 6 will be considered, where the elastic part is shifted as the load is increased beyond the yield point.

From the finite element model the maximum stresses and strains occur on the bottom surface because of stress concentration at the edge of the hole on the center connections. When loading is removed the stresses return to zero and permanent plastic deformation remains.

The fatigue process is a function of several variables depending on the fatigue model used. These models include maximum normal stress and strain amplitude, octahedral shear stress amplitude and mean stresses. Notice that fatigue damage is independent of mean strains and hence, independent of total plastic deformation. Since loading and unloading do not cause further plastic deformation on any given loading sublevel, one is left with the elastic part of the cyclic hysteretic loop in Fig. 6.

4.2 Material parameters for fatigue analysis

In a strain-life curve, the strain amplitude ε_a is assumed as the sum of elastic and plastic components in the form (Coffin 1971)

$$\varepsilon_a = \frac{\sigma'_f}{E}\left(2N_f\right)^b + \varepsilon'_f\left(2N_f\right)^c \tag{1}$$

where ε'_f is the true fracture strain; σ'_f is the true fracture stress; N_f is the number of cycles to failure under alternating load; b is the slope of the elastic part; and c is the slope of the plastic part of the strain-life curve on a logarithmic plot. If the plastic component on the right side of Eq. (1) is eliminated and both sides are multiplied by E assuming linearly elastic behavior, then the classical stress-life equation is obtained in the form

$$\sigma_a = \sigma'_f\left(2N_f\right)^b \tag{2}$$

where σ_a is the alternating stress. Eq. (2) is the basic stress-life equation that is used to calculate fatigue life for completely reversed cycles.

In order to use this equation, the two parameters σ'_f and b, which are not provided in the ASTM standard, need to be evaluated. The first one is the true fracture strength or fatigue strength coefficient and the second one is the slope of the log-log plot of the elastic component of the equation or the fatigue strength exponent. These two parameters are approximated by the universal slopes method (Manson 1965) and correlated to monotonic tensile test parameters. Values of

$$\sigma'_f = 1.902\sigma_u \text{ and } b = -0.12 \tag{3}$$

were used in this work, where σ_u is the ultimate strength.

4.3 Variables at each loading level

Kinematic assumptions. Considering a linear response between load and displacement in the elastic loading and unloading zone defined in Fig. 6, linear kinematic (strain-displacement) relations for ε_a were obtained in terms of the load magnitude P in Eq. (4). Kinematic non-linearity in geometry is used to account for large displacements in the non-linear finite element representation while these equations are used to calculate the fatigue life within loading levels.

$$\varepsilon_a = \frac{\varepsilon_{max}}{2}\left(1 - \frac{P_{min}}{P_{sub\,max}}\right) \quad if \quad \varepsilon_{max} \leq \varepsilon_y$$

$$\varepsilon_a = \frac{\varepsilon_y}{2}\left(1 - \frac{P_{min}}{P_{sub\,max}}\right) \quad if \quad \varepsilon_{max} > \varepsilon_y \quad and \quad P_{sub\,max} \geq P_{max} \tag{4}$$

$$\varepsilon_a = \frac{\varepsilon_y}{2}\left(\frac{P_{sub\,max} - P_{min}}{P_{max}}\right) \quad if \quad \varepsilon_{max} > \varepsilon_y \quad and \quad P_{sub\,max} < P_{max}$$

where ε_y is the strain at first yield; ε_{max} is the maximum principal strain obtained from the finite element analysis; P_{max} is the previously applied maximum load starting from the first loading

Table 3 Fatigue analysis of Configuration #3. Details of this configuration are given in Table 1. First failure was observed at D4. $\sigma'_f = 1.902 \, \sigma_u$ and $b = -0.12$

	$\Delta\varepsilon_{max}$ $\times 10^{-3}$	σ_m	σ_{max}	n	N_M	N_{SWT}	N_G	F_M	F_{SWT}	F_G
A1	1.138	129.7	259.4	2000	19182	14576	10065	0.149	0.196	0.284
A2	1.138	129.4	258.8	3500	19652	14715	10065	0.403	0.536	0.781
A3	1.138	129.4	258.8	1000	19652	14715	10065	0.476	0.633	0.923
A4	1.138	129.4	258.8	250	19652	14715	10065	0.494	0.657	0.958
A5	0.285	97.1	129.4	2000	3599611629	85235994	#	0.494	0.657	0.958
A6	0.569	129.4	194.1	2000	6338445	876229	3246250	0.495	0.660	0.959
A7	0.854	161.8	258.8	125	117751	48789	30063	0.496	0.664	0.965
A8	0.569	194.1	258.8	125	1795078	264265	188072	0.496	0.665	0.966
B2	0.717	80.9	161.8	2500	2274833	715038	2599950	0.498	0.670	0.967
B3	1.070	121.3	242.6	750	38902	24917	23176	0.525	0.713	1.013
B4	1.138	129.4	258.8	250	19652	14715	10065	0.544	0.737	1.049
B6	0.569	129.4	194.1	1750	6338445	876229	3246250	0.544	0.740	1.050
B7	0.854	161.8	258.8	125	117751	48789	30063	0.546	0.744	1.056
B8	0.569	194.1	258.8	125	1795078	264265	188072	0.546	0.744	1.057
C2	0.683	77.6	155.3	1250	3369887	1038694	4031757	0.546	0.746	1.057
C3	1.029	116.5	232.9	750	59566	34756	38710	0.564	0.777	1.085
C4	1.138	129.4	258.8	250	19652	14715	10065	0.582	0.801	1.120
C6	0.569	129.4	194.1	1500	6338445	876229	3246250	0.583	0.804	1.121
C7	0.854	161.8	258.8	125	117751	48789	30063	0.584	0.807	1.127
C8	0.569	194.1	258.8	125	1795078	264265	188072	0.584	0.808	1.128
D2	0.668	75.5	151.0	1250	4415806	1283022	5444514	0.585	0.809	1.128
D3	0.994	113.2	226.5	500	79725	45130	54824	0.594	0.825	1.141
D4	1.138	129.4	258.8	250	19652	14715	10065	0.612	0.849	1.177

sublevel being zero at the first sublevel; $P_{sub\,max}$ is the maximum sublevel load; and P_{min} is the minimum sublevel load. The loading level and sublevel definition refer to the loading sequence in Fig. 3, where loading levels are defined ranging from *A* to *E* in order of increasing load *P* and loading sublevels are defined from 1 through 8 in the load sequence shown in the figure.

The maximum stress σ_{max} was found for each loading sublevel by using proportionality equations for stress in the elastic zone similar to Eq. (4)

$$\sigma_{\max} = \sigma_{\max p} \quad if \quad P_{sub\max} \geq P_{\max}$$

$$\sigma_{\max} = \sigma_{\max prev} \frac{P_{sub\max}}{P_{\max}} \quad if \quad P_{sub\max} < P_{\max} \tag{5}$$

where σ_{maxp} is the maximum stress, and $\sigma_{maxprev}$ is the maximum previously applied stress, and their value depend on the specific model adopted to take mean stress effect into account. As explained in Section 4.4, principal stresses are used in the SWT and Morrow models, whereas the the von Mises stress is adopted in the Goodman approach.

For example, consider the results in Table 3, for which a reference load P (given in Table 1) is assumed.

At the first level (A) and the first sublevel (1), identified as A1 in column 1 of Table 3, the protocol in Fig. 3 indicates that $n = 2000$ cycles between 0 and 0.25P should be applied. The finite element analysis provides values of $\varepsilon_{\max} = 4.049 \times 10^{-3}$; and stresses with $\sigma_{\max} = 259.4$ MPa as shown in Table 3 with $\sigma_m = (\sigma_{\max} + \sigma_{\min})/2 = 129.7$MPa. Because this is the first sublevel, the previously applied maximum load $P_{\max} = 0$; whereas $P_{sub\max} = 0.25P$. Then, since $\varepsilon_{\max} > \varepsilon_y$ and $P_{sub\max} > P_{\max}$ Eq. (4) yields $\varepsilon_a = \varepsilon_y/2$, which remains unchanged until sublevel A4.

For sublevel A5, which has 2000 oscillations between 0.25P and 0.5P. The previously applied maximum load $P_{\max} = P$ and $P_{sub\max} = 0.5P$. Then, since $\varepsilon_{\max} > \varepsilon_y$ after fist yield and $P_{sub\max} < P_{\max}$,

Eq. (4) yields $\varepsilon_a = \dfrac{\varepsilon_y}{2}\left(\dfrac{0.5P - 0.25P}{P}\right) = 0.125\varepsilon_y = 1.423 \times 10^{-4}$ and $\Delta\varepsilon_{\max} = 2\varepsilon_a = 0.285 \times 10^{-3}$ in

Table 3. Regarding stresses, $\sigma_{\max} = 129.4$ MPa from Eq. 5 and Table 2 and $\sigma_m = (\sigma_{\max} + \sigma_{\min})/2 = 97.1$ MPa.

The stresses and strains in Table 3 are recorded for each sublevel of the loading protocol for which the load exceeds the previously applied maximum load starting from the first loading sublevel. As an example, consider loading level A in Fig. 3. In this case only loading sublevels A1, A2, A3 and A4 were recorded since A5, A6, A7 and A8 do not exceed the load in sublevel A4. The next sublevel would be B4 because it exceeds the load in A4.

Notice from Eq. (4) that after first yield the strain amplitude becomes independent of the maximum principal strain and only depends on the loading sequence. Similar proportionality equations for strain amplitude were used for the strain-hardening material definition by accounting for the strain hardening zone and assuming the loading and unloading path to be linear and parallel to the elastic zone.

4.4 Mean stress effect

Three criteria are considered in this section in order to take mean stress effects into account. Morrow (1965) proposed to modify the number of cycles to failure as follows

$$N_f = N_M \left(1 - \frac{\sigma_m}{\sigma'_f}\right)^{1/b} \tag{6}$$

where σ_m is the mean alternating stress; N_M is the number of cycles to failure according to this criterion. Substituting for N_f in Eq. (1) gives

$$\varepsilon_a = \frac{\sigma'_f}{E}\left(1 - \frac{\sigma_m}{\sigma'_f}\right)(2N_M)^b + \varepsilon'_f\left(1 - \frac{\sigma_m}{\sigma'_f}\right)^{c/b}(2N_M)^c \tag{7}$$

Upon eliminating the plastic component, one is left with the stress-life relationship

$$\sigma_a = \left(\sigma'_f - \sigma_m\right)(2N_M)^b \tag{8}$$

which includes the mean stress effect. Here the stress amplitude and mean stress are calculated from the major principal stress.

The second approach considered in this work is originally attributed to Goodman, who proposed the following relation for addressing mean stresses

$$\frac{\sigma_a}{\sigma_{am}} + \frac{\sigma_m}{\sigma_u} = 1 \tag{9}$$

where σ_{am} is the equivalent stress amplitude for completely reverse loading that addresses the mean stress effect and the stress amplitude and mean stress are calculated from the von Mises stress. Using the classical stress-life equation in terms of σ_{am}

$$\sigma_{am} = \sigma'_f\left(2N_G\right)^b \tag{10}$$

N_G is the modified number of cycles to failure in this criterion Substituting for σ_{am} from Eq. (9) leads to

$$\sigma_a = \sigma'_f\left(1 - \frac{\sigma_m}{\sigma_u}\right)(2N_G)^b \tag{11}$$

The Morrow equation is similar to that due to Goodman, except for using the true fracture stress instead of the ultimate strength.

The third approach considered to account for mean stress effects is based on the work of Smith *et al.* (1970), known as SWT, which was developed for materials that fail predominantly on maximum tensile stress or strain planes. According to SWT the life for any situation of mean stresses depends on the product of maximum stress times strain amplitude on the principal plane, and the resulting equation is

$$\sigma_{\max}\varepsilon_a = \frac{\left(\sigma'_f\right)^2}{E}\left(2N_{SWT}\right)^{2b} + \sigma'_f\,\varepsilon'_f\left(2N_{SWT}\right)^{b+c} \tag{12}$$

where $\sigma_{\max}$ is the major principal stress; and N_{SWT} is the corresponding number of cycles to failure in this criterion. Upon eliminating the plastic component of strain, the SWT equation results in

$$\sigma_{\max}\varepsilon_a = \frac{\left(\sigma'_f\right)^2}{E}\left(2N_{SWT}\right)^{2b} \tag{13}$$

The number of cycles to failure was found for each loading sublevel by solving for N in Eqs. (8), (11) or (13). They are reported in the calculations of columns 6-8 in Table 3.

4.5 Fatigue damage

The Palmgren-Miner rule is used in order to take into account variable amplitude loading

$$\sum_i \frac{n_i}{(N_f)_i} = 1 \tag{14}$$

where n is the number of cycles at the stress level i at which N_f cycles would cause failure. Palmgren-Miner's linear damage rule has some limitations because the order in which distinct amplitude cycles are applied in reality is found to have an effect on fatigue damage (Liu and Mahadevan 2007). Mahendran and Mahaarachchi (2002) suggested that Miner's rule should be modified in order to take into account experimental evidence from multilevel cyclic tests performed on claddings. The modified Miner's rule is as follows

$$F = \sum_i \frac{1}{K} \frac{n_i}{(N_f)_i} \tag{15}$$

where K is a modification factor equal to 0.7 and F equals the fatigue damage, being zero for no damage and 1 for 100% damage, in which case the fatigue life or number of cycles to failure has been reached. This summation is continued for each loading level until the fatigue damage F exceeds 1 indicating that failure has occurred. Once the fatigue damage is calculated, the location chosen for reading the stresses and strains, which is the same for every loading sublevel, was found to yield the highest fatigue damage F.

The fatigue damage definition of Eq. (15) has been adopted in this work.

As mentioned before, the stresses and strains in Eqs. (4) and (5) are determined for each configuration from the finite element analysis (as described in Section 3) at a location where fatigue damage F is maximum. This is the location where fatigue failure first occurs (i.e., for which $F \geq 1$) which may be the location with the highest stresses. Several locations may have to be calculated around the high stress area in order to determine the location of highest fatigue damage F since the loading sequence may prevent for the fatigue damage to accumulate in a linear fashion.

4.6 On fatigue process

Fatigue data collected for different materials shows that the fatigue process may be divided into three regions: nucleation, shear, and tension (Socie and Marquis 2000). The extent of each region in the fatigue life depends on the material and type of loading. As a result the choice of the fatigue model will also depend on these factors. Empirical evidence shows that at a high number of cycles, fatigue is dominated by tension and at low numbers by shear (Hua and Socie 1985, Socie *et al*. 1989, Bannantine and Socie 1985). Also at high lives or number of cycles, fatigue is dominated by elastic deformation as compared to plastic deformation at low lives as predicted by Eq. (1). Upon this premise it can be concluded that tension damage is dominated by elastic deformation and shear damage by plastic deformation. This behavior is also seen in brittle materials, which fail in tension with no plastic deformation, as opposed to more ductile materials, which fail predominantly in shear and exhibit large plastic deformation.

The above discussion applies for completely reversed cycles with zero mean stress. Recent research in tropical cyclone simulation shows that minimum cyclic wind pressure is greater than
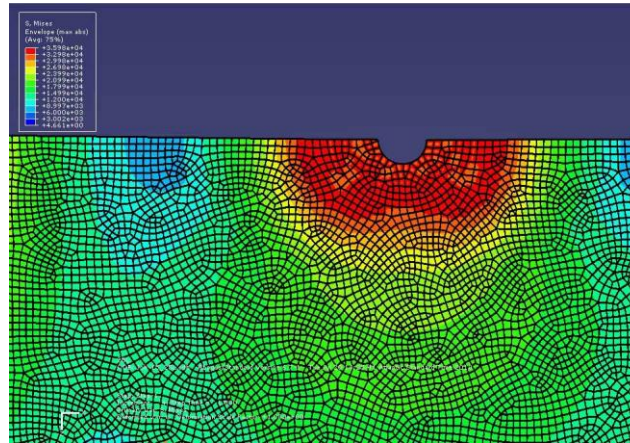
Fig. 7 Von Mises stresses at bottom surface from a typical center screwed connection

zero, thus the stress ratio *R* and the mean stress are also greater than zero (Henderson *et al*. 2009). In view of the nature of cyclonic wind loading, in which there is a mean stress and only tension loading is considered, fatigue will be dominated by elastic deformation at low number of cycles. This is a direct consequence of the mean stress effect, given that mean stresses increase the fatigue damage caused by elastic deformation at low number of cycles. As a result damage will be accumulated in the low cycle range and failure will occur before reaching the high cycle range. Evidence shows that such low cycle fatigue failures occur within 10,000 load cycles and less than 60% of the components static strength, and is characterized by rapid brittle failure (Henderson *et al*. 2008).

Recent studies in the fatigue life prediction of aluminum plate specimens with fastener holes show that the accuracy of any multiaxial fatigue criterion depends on loading nature in terms of torque tightening load of the fasteners and cold-expanded pre-stresses (Chakherlou and Abazadeh 2011). Multiaxial fatigue criteria were developed and tested over the years (Smith *et al*. 1970, Crossland 1956, Brown and Miller 1973, Fatemi and Socie 1989, Glinka *et al*. 1995, Wang and Yao 2006, Li *et al*. 2009). These criteria involve a combination of shear and normal stress and strain parameters. Brown and Miller (1973), Fatemi and Socie (1989), which were developed predominantly for shear damage, require tension and torsion fatigue test data, which is not readily available. Since fatigue damage occurs at the edge of the screw hole, where tensile hoop stresses are maximum and the stress normal to the hoop direction is zero, the multiaxial stress state reduces to a uniaxial stress state. As a result and in light of the cyclonic wind loading nature, in which fatigue damage is dominated by elastic deformation under tension loading, models such as SWT which only involve a normal stress and strain parameter representing the uniaxial stress state will later be shown to work better in predicting the fatigue life.

5. Fatigue damage results and discussion

A comparison of fatigue models is presented with reference to Fig. 8, in which the number of cycles to failure is N_M for Morrow, N_G for Goodman, and N_{SWT} for the Smith, Watson and Topper method. To carry out the calculations, a mean stress of 113.8 MPa was used, which is half of the
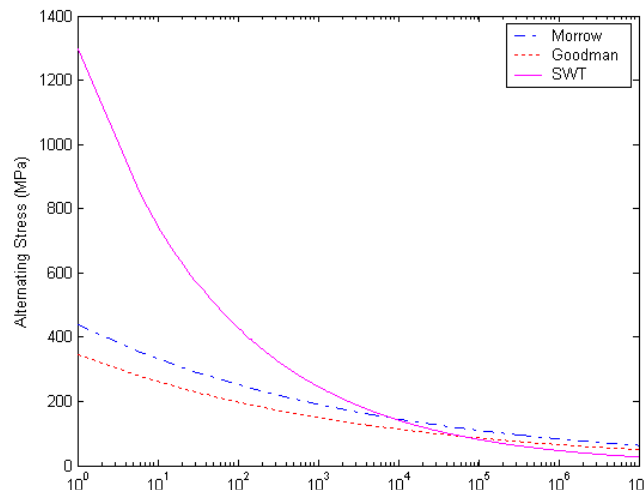
Fig. 8 Comparison of Fatigue Models for the universal slopes method

yield strength, and the universal slopes method. The horizontal line crosses the curves at an alternating stress equal to the mean stress of 113.8 MPa for tension loading. At this alternating stress, the results of the SWT method fall between the Goodman and Morrow equations.

The Goodman approach is the most conservative model taking into account that it provides good results for brittle materials and is more conservative for ductile materials.

Table 3 has been calculated using the preceding methodology, for one specific specimen identified as # 3 in Table 1. Column 1 is the strain range or two times the strain amplitude as defined in Section 4. Columns 2 and 3 are the mean and maximum stresses from Eq. (5). Column 4 is the number of cycles on each loading sublevel as defined in Fig. 3.

The sequence of computations is as follows: Columns 5, 6, and 7 are calculated from Eqs. (8), (13) and (11), and Columns 8, 9 and 10 are calculated from Eq. (15). Each row is computed for the stress and strain state in a given loading sublevel. Computations are made until loading sublevel D4 where first connection failure is reported by García-Palencia and Godoy (2013) in Configuration #3.

Fig. 9 shows the fatigue damage determined from Eq. (15) for the 12 configurations in experiments performed by García-Palencia and Godoy (2013), calculated and plotted at the middle of the loading sublevel in which failure was observed. The triangle, square and diamond symbols in Fig. 9 stand for the Goodman, SWT, and Morrow fatigue models described in Section 4 respectively. Results were obtained for the elastic-plastic material definition described in Section 3. The figure shows that the Goodman model is slightly dependent on the loading level increasing in fatigue damage at higher levels. Since the Goodman model uses the von Mises stress, which becomes constant after the yield point is reached, the alternating stress will only depend on the loading sequence as predicted by the kinematic assumptions in Section 4. For the other two models, in which the stresses and strains are not constant after first yield, there is no apparent dependence.

Fig. 10 shows the same results as Fig. 9 but taking the strain hardening material definition of Section 3 into account. Fig. 10 shows more scattering around the expected value of $F = 1$ than the
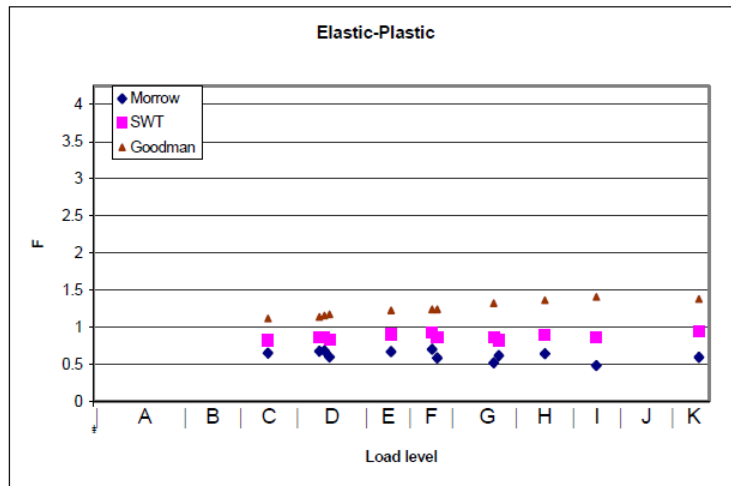
Fig. 9 Comparison of fatigue models for the elastic-plastic material definition
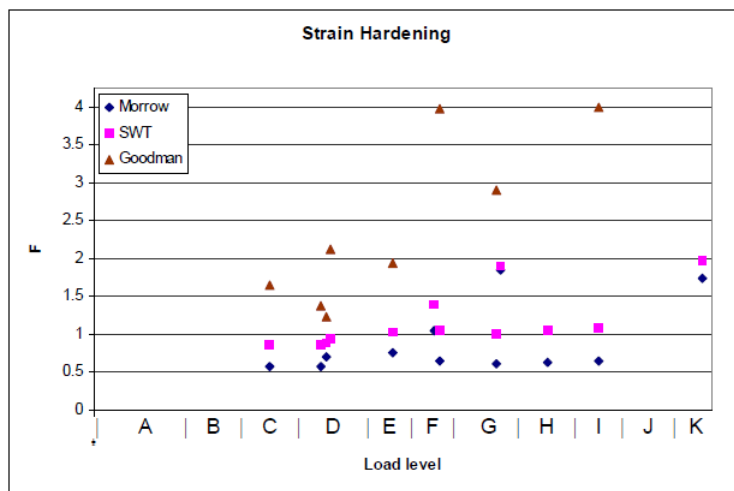
Fig. 10 Comparison of fatigue models for the strain hardening material definition

results shown in Fig. 9, especially for the Goodman model since the von Mises stress used by Goodman is directly related to the material definition. From these two figures, it may be concluded that the elastic-plastic material definition provides a better correlation for all three of the fatigue models than the strain hardening material definition since the fatigue damage F seems to be independent of the loading sublevel in which failure was observed in Fig. 9.

Fig. 11 is an expansion of Fig. 9 and Table 4 lists the average and standard deviation of the fatigue life computed for each model. From the last row of Table 4 it is concluded that SWT provides the best correlation with a value of dispersion of nearly half of the other two fatigue models, most likely because SWT uses a stress and strain parameter adequately representing the uniaxial stress state described in Section 4.6 and was developed specifically for tension damage.

Fig. 12 shows the SWT approach of Fig. 11 for the different types of connections. From Fig. 12 it is concluded that the fatigue damage calculated is independent of the type of connection, number
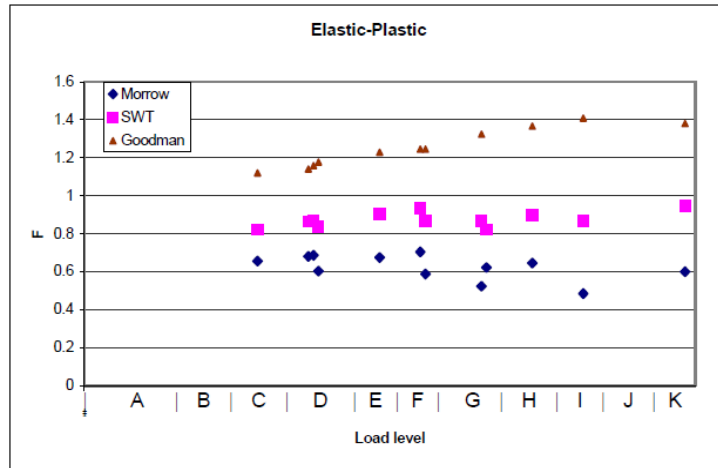
Fig. 11 Comparison of fatigue models for the elastic-plastic material definition
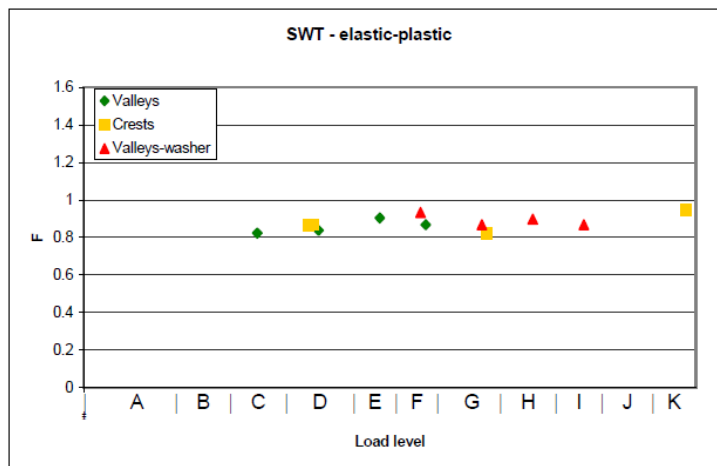
Fig. 12 Comparison of connection types and fatigue damage

Table 4 Fatigue damage average and standard deviation for the 12 configurations

	Goodman	Morrow	SWT
μ	1.269	0.623	0.875
s	0.1296	0.0671	0.0392
s/μ	0.1021	0.1078	0.0448

of connections and configuration, meaning that the SWT - elastic-plastic model works well for all 12 configurations predicting an average fatigue damage of 0.875. This value suggests that the fatigue parameters should be modified in order to fit the experimental data for which the expected fatigue damage is 1.

Studies by Park and Song (1995) show that the fatigue strength exponent or slope of the elastic part of the strain-life curve b is observed to vary over a relatively wide range and to be material dependent. The same study also shows the universal slopes method to give slightly non-
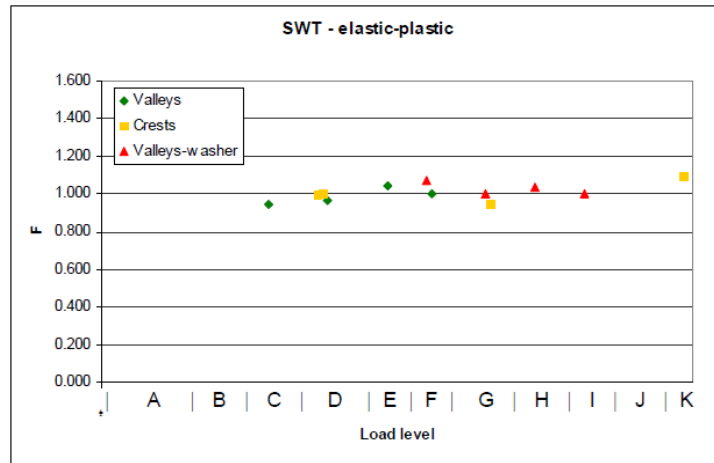
Fig. 13 Comparison of connection types and fatigue damage for the proposed method (Table 5). $\sigma'_f = 1.87\sigma_u$ and $b = -0.12$
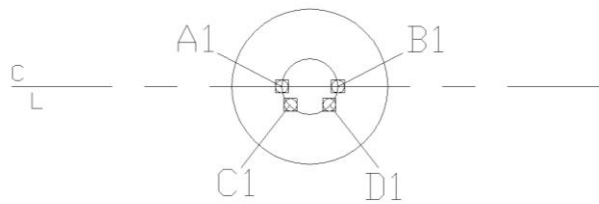
Fig. 14 Location of points where fatigue failure occurs

Table 5 Fatigue damage calculated at the middle of the loading sublevel in which failure was observed by García-Palencia and Godoy (2013). $\sigma'_f = 1.87\sigma_u$ and $b = -0.12$

Configuration number (Garcia-Palencia and Godoy 2013)	Fatigue damage F_{SWT}	Location in plan, with reference to Fig. 1	Location around the screw, with reference to Fig. 14
3	0.964	5	A1
4	1.000	6	A1
5	1.035	6	B1
6	1.075	4	B1
13	1.041	4	B1
15	0.948	4	B1
17	1.000	4	B1
18	1.000	4	B1
19	1.089	5	B1
20	0.996	3	B1
21	1.000	5	D1
24	0.948	5	B1

conservative predictions at short lives, which is the case here. In order to overcome the difficulty associated in determining these parameters, the fatigue strength coefficient σ'_f was approximated

by fitting the SWT fatigue model to the experimental data, leading to

$$\sigma'_f = 1.87\sigma_u \quad and \quad b = -0.12 \tag{16}$$

By using this correlation instead of the universal slopes method, the method described for SWT should yield results within a given accuracy for similar materials under tension loading.

As a result the fatigue life F can be determined analytically with just the monotonic tensile parameters of the material. The fatigue damage calculated at the middle of the sublevel of the observed failure for the 12 configurations and for the proposed method varies between 0.948 and 1.089 damage with a mean of 1 and sample standard deviation of 0.0448. This is the difference in fatigue damage between the experimental result and the computed result. Notice that the fatigue damage calculated for SWT at row D4 of Table 3 increased from 0.849 to 0.964 by using equation 16 instead of Eq. (3) as shown in Table 5.

By using the *t*-distribution for small samples ($n = 12$) and the mean and sample standard deviation of the calculated fatigue damage, the range in fatigue damage for a 90% probability of failure is ± 0.023. For the proposed model to predict failure with a 90% confidence, the calculated fatigue damage should fall between 0.977 and 1.023 or, if an upper limit is not used, 0.982 or higher. As a result the confidence interval in the number of cycles to failure for specimens that will fail in 10,000 constant amplitude cycles, which is typical for the assumed wind loading protocol, is ± 230 cycles for 9 failures out of 10 tests. This interval falls within the number of cycles of most loading sublevels of the loading sequence used and provides evidence that the proposed fatigue model will accurately predict the loading sublevel at which failure occurs for 9 out of 10 specimens. This confidence interval represents experimental measurement uncertainty because the exact number of cycles to failure was not recorded and only the loading sublevel, inherent uncertainty associated with the fatigue process, and fatigue model precision.

Once the fatigue capacity of the connection has been reached, it is expected that cracks may start to form and grow until failure occurs. Once a crack forms, it grows in mode I as predicted by previous studies (Socie and Marquis 2000). Under mode I loading a crack grows perpendicular to the major principal strain direction, which is always tangent to the screw hole. The finite element model shows that the location where the major principal strain is maximum is not the same for all 12 configurations, meaning that the direction of crack propagation depends on the number of screwed connections, the thickness of the cladding, and the type of connection.

Fig. 14 shows typical locations where fatigue failure occurs, identified as A1, B1, C1 and D1. For each configuration studied in this work, fatigue damage has been calculated in Table 5 at the middle of the loading sublevel in which failure was observed in the experiments (García-Palencia and Godoy 2013). For each configuration, the location in plan (as given in Fig. 1) is indicated, together with the location around the screw (as given in Fig. 14). This is consistent with results obtained in the experiments of García-Palencia and Godoy (2013), where cracks developed perpendicular to the screw hole at a location predicted by this study.

6. Conclusions

In this research the stresses and strains that are responsible for failures of steel cladding at the connections were investigated using finite element analysis. The companion study of García-Palencia and Godoy (2013) approached this problem based on full-scale testing under alternating loads. A recent loading protocol established by the Canadian Standards Association was

implemented in both experiments and computations for rating a specific structure according to the level of wind damage it can withstand.

A method for the fatigue life prediction of steel thin-walled folded plates was developed using a computational followed by an analytical approach. A computational analysis at the structural level was used to evaluate stresses under an assumed representation of the loads in the testing procedure. The stress and strain fields thus computed were subsequently employed in an analytical fatigue analysis. Because a number of fatigue criteria have been reported in the literature, some of them were compared by numerical experiments and one was selected based on its capacity to predict the fatigue damage associated with wind fluctuations. The fatigue criteria employed have been reported by other authors in the literature, and the novelty here is the application of such criteria as part of a computational-analytical methodology oriented to represent fatigue failure under a dynamic load protocol.

This method requires only the monotonic tensile properties of the material, and allows predicting a fatigue failure mechanism for different types of connections, thickness, and configurations.

A finding of this research is that loading sublevels with less amplitude than in previous levels cause less damage because elastic deformation is less after permanent plastic deformation, thus requiring a larger load than before in order to reach the yield strength. This results from the fact that the original geometry changes to a stiffer configuration after plastic deformation. This can be seen to be the case in Table 3, where most of the damage is in the first four loading sublevels. By comparing the fatigue damage between screwed connections in valleys and the same connections reinforced with washers on the same loading sublevel, it is found that adding a washer increases the fatigue life of the connection by an average of 18%. As a result a non-reinforced connection that fails at 100 constant amplitude cycles will now fail at 118 cycles when reinforced with a washer.

This increase in the fatigue life computed from first connection failure is also shown by García-Palencia and Godoy (2013) as a function of the ultimate load determined for progressive failure of at least three connections. Although García-Palencia and Godoy (2013) found that ultimate load capacity (failure of three connections) is almost doubled by adding a washer, in this study (based on first connection failure) it was found that the number of cycles as well as the others parameters considered are also necessary for determining the fatigue performance of a given configuration.

Acknowledgements

References

ABAQUS (2008), ABAQUS v6.8, Simulia, Dassault Systemes, Warwick, RI, USA.
ASTM (2009), Standard Specification for Steel Sheet, Zinc-Coated (Galvanized) or Zinc-Iron Alloy-Coated (Galvannealed) by the Hot-Dip Process, ASTM-A653-09, American Society for Testing and Materials,

West Conshohocken, PA, USA.

Bannantine, J.A. and Socie, D.F. (1985), "Observations of Cracking Behavior in Tension and Torsion Low Cycle Fatigue", ASTM STP 942, American Society for Testing and Materials, West Conshohocken, PA.

Baskaran, A., Molleti, S. and Sexton, M. (2006), "Wind performance evaluation of fully bonded roofing assemblies", *Construct. Build. Mater.*, **22**, 1-21.

Beck, V.R. and Stevens, L.K. (1979), "Wind loading failures of corrugated roof cladding", *Civil Eng. Trans.*, **21**(1), 45-56.

Brown, M.W. and Miller, K.J. (1973), "A theory for fatigue under multiaxial stress-strain conditions", *Proc. Inst. Mech. Eng.*, **187**, 745-756.

Chakherlou, T.N. and Abazadeh, B. (2011), "Estimation of fatigue life for plates including pre-treated fastener holes using different multiaxial fatigue criteria", *Int. J. Fatigue*, **33**, 343-353.

Coffin, L.F. Jr. (1971), "A note on low cycle fatigue laws", *J. Mater.*, **6**(2), 388-402.

Crossland, B. (1956), "Effect of large hydrostatic pressures on the torsional fatigue strength of an alloy steel", *Proceedings of the international conference on fatigue of metals, Institution of Mechanical Engineers*, London.

Fatemi, A. and Socie, D.F. (1989), "Multiaxial fatigue damage mechanisms and life predictions", *Advances in Fatigue Science and Technology*, Eds. C. Moura-Branco and L. Guerra-Rosa, Kluwer, Dordrecht, The Netherlands.

García, R. (2007), "Development of hurricane based fragility curves for wood-zinc houses in Puerto Rico", PhD Thesis, University of Puerto Rico at Mayagüez, Mayagüez, Puerto Rico.

García-Palencia, A.J. and Godoy, L.A. (2013), "Fatigue experiments on steel cold-formed panels under a dynamic load protocol", *J. Struct. Eng. Mech.*, **46**(3), 387-402.

Glinka, G., Shen, G. and Plumtree, A. (1995), "A multiaxial fatigue strain energy density parameter related to the critical plane", *Fatigue Fract. Eng. Mater. Struct.*, 18, 37-46.

Henderson, D., Ginger, J., Berndt, C. and Kopp, G.A. (2008), "Fatigue failure of G550 steel building components during wind loading", *Proc. Australasian Engineering Conference*, June.

Henderson, D.J., Ginger, J.D., Morrison, M.J. and Kopp, G.A. (2009), "Simulated tropical cyclonic winds for low cycle fatigue loading of steel roofing", *Wind Struct.*, **12**(4), 381-398.

Hua, C.T. and Socie, D.F. (1985), "Fatigue damage in 1045 steel under variable amplitude loading," *Fatigue Fract. Eng. Mater. Struct.*, **8**(2), 101-104.

Lee, K.H. and Rosowsky, D.V. (2004), "Fragility assessment for roof sheathing failure in high wind regions", *Eng. Struct.*, **27**, 857-868.

Li, J., Zhang, Z.P., Sun, Q. *et al*. (2009), "A new multiaxial fatigue damage model for various metallic materials under the combination of tension and torsion loadings", *Int. J. Fatigue*, **31**, 776-781.

Liu, Y. and Mahadevan, S. (2007), "Stochastic fatigue damage modeling under variable amplitude loading", *Int. J. Fatigue*, **29**, 1149-1161.

López, H.D. and Godoy, L.A. (2005), "Metodología para la estimación de daños estructurales ocasionados por vientos huracanados en edificaciones industriales", *Revista Int. de Desastres Naturales, Accidentes e Infraestructura Civil*, **5**(2), 121-134. (in Spanish)

Mahaarachchi, D. and Mahendran, M. (2008), "A strain criterion for pull-through failures in crest-fixed steel claddings", *Eng. Struct.*, **31**, 498-506.

Mahaarachchi, D. and Mahendran, M. (2009), "Wind uplift strength of trapezoidal steel cladding with closely spaced ribs", *J. Wind Eng. Indus. Aerodyn.*, **97**, 140-150.

Mahendran, M. (1995), "Wind-resistant low-rise buildings in the tropics", *ASCE J. Perform. Constr. Facil.*, **9**, 330-346.

Mahendran, M. and Mahaarachchi, D. (2002), "Cyclic pull-out strength of screwed connections in steel roof and wall cladding systems using thin steel battens", *ASCE J. Struct. Eng.*, **128**(6), 771-778.

Mahendran, M. and Mahaarachchi, D. (2004), "Splitting failures in trapezoidal steel roof cladding", *ASCE J. Perform. Constr. Facil.*, **18**, 4-11.

Mahendran, M. and Tang, R.B. (1998), "Pull-out strength of steel roof and wall cladding systems", *ASCE J. Struct. Eng.*, **124**(10), 1192-1201.

Manson, S.S. (1965), "Fatigue: a complex subject - some simple approximations", NASA-TM-X-52084, National Aeronautics and Space Administration.

Matcor (2007), *Rolled Formed Metal Building Components*, Matcor, Inc. Guaynabo, Puerto Rico.

Morrow, J. (1965), Cyclic Plastic Strain Energy and Fatigue of Metals, Internal Friction, Damping and Cyclic Plasticity, ASTM STP 378, American Society for Testing and Materials, West Conshohocken, PA.

Park, J.H. and Song, J.H. (1995), "Detailed evaluation of methods for estimation of fatigue properties", *Int. J. Fatigue*, **17**(5), 365-373.

Prinz, G.S. and Nussbaumer, A. (2012), "Fatigue analysis of liquid-storage tank shell-to-base connections under multi-axial loading", *Eng. Struct.*, **40**, 75-82.

Salmon, C.G., Johnson, J.E. and Malhas, F.A. (2009), *Steel Structures Design and Behavior*, Fifth Edition, Pearson Prentice Hall, Saddle River, NJ. USA.

Smith, R.N., Watson, P. and Topper, T.H. (1970), "A stress-strain parameter for the fatigue of metals", *J. Mater.*, **5**(4), 767-778.

Socie, D.F., Kurath, P. and Koch, J.L. (1989), *A Multiaxial Fatigue Damage Parameter*, European Group on Fracture, EGF Publication 3, Mechanical Engineering Publications, London.

Socie, D.F. and Marquis, G.B. (2000), *Multiaxial Fatigue*, Society of Automotive Engineers, Philadelphia, PA, USA.

Wang, Y.Y. and Yao, W.X. (2006), A multiaxial fatigue criterion for various metallic materials under proportional and non-proportional loading", *Int. J. Fatigue*, **28**, 401-408.